Environmental Science: Atmospheres

ROYAL SOCIETY OF CHEMISTRY

PAPER

View Article Online
View Journal | View Issue

Open Access Article. Published on 08 November 2025. Downloaded on 2/14/2026 3:37:43 AM.
This article is licensed under a Creative Commons Attribution 3.0 Unported Licence.

Check for updates

Cite this: *Environ. Sci.: Atmos.*, 2026, **6**, 90

Diaterpenylic acid acetate (DTAA): characterization and OH oxidation in atmospheric chambers

Kalliopi Florou,[a] Spiro Jorga,[†b] Agata Blaziak,[c] Christina N. Vasilakopoulou,[a] Petro Uruci,[ad] Rafal Szmigielski[c] and Spyros N. Pandis[*ad]

Diaterpenylic acid acetate (DTAA) ($C_{10}H_{16}O_6$) is a later-generation biogenic secondary organic aerosol (OA) component, formed during the oxidation of first-generation products of monoterpenes such as α-pinene, and β-pinene. Identified in aerosol in terrestrial and forested environments, DTAA is a product of the oxidation of both terpenylic acid and 1,8-cineole. Here, we present the first comprehensive chamber study investigating DTAA's volatility, gas–particle partitioning, and oxidative transformation under atmospherically relevant conditions through a combination of laboratory measurements, modeling, and chemical analysis. Its physicochemical properties were characterized by using two atmospheric simulation chambers, equipped with a range of particle and gas-phase instrumentation. A high-resolution time-of-flight aerosol mass spectrometer (HR-ToF-AMS) identified DTAA aerosol characteristic peaks at mass-to-charge (*m*/*z*) 59, 67, 79, 91, 95, 101, 114 and 139. DTAA aerosol density was estimated to be 1.3 ± 0.2 g cm^{-3}. DTAA was classified as a semi-volatile organic compound (SVOC), with a saturation concentration of 3.6–3.9 μg m^{-3}. Upon hydroxyl (OH) radical exposure, DTAA underwent significant chemical aging, producing secondary organic aerosol (SOA) with distinct spectral features and a little higher oxygen-to-carbon ratio (O : C = 0.63). The AMS spectrum of the produced SOA was quite different from that of pure DTAA (R^2 = 0.48 or θ = 31°) and resembled to an extent (θ = 14–20°), the spectra of ambient biogenic SOA. A suite of oxidation products were identified *via* proton transfer reaction mass spectrometry (PTR-MS) and chemical ionization mass spectrometry (CIMS) ranging from small molecules (*e.g.* acetone) to multifunctional species. A kinetic model incorporating partitioning, wall loss, and oxidation accurately captured SOA production during the DTAA reaction with OH, assuming an effective fragmentation probability of 32%. These results highlight the atmospheric relevance of DTAA as a reactive SVOC and underline the importance of integrating later generation chemical processes in SOA studies.

Received 29th July 2025
Accepted 6th November 2025

DOI: 10.1039/d5ea00086f

rsc.li/esatmospheres

Environmental significance

This study investigates the oxidation of DTAA by OH radicals. DTAA can be viewed as a model later-generation product of monoterpene ozonolysis, a major source of secondary organic aerosol on both regional and global scales. This paper shows that DTAA is semivolatile and continues reacting, producing even later-generation products. Even at this late reaction stage, functionalization is the major reaction pathway, average SOA O : C increases and SOA mass increases or decreases depending on temperature. The results show how dynamic the SOA production system is and how important the later-generation processes are for its chemical and physical characteristics.

1 Introduction

Biogenic volatile organic compounds (bVOCs) are a class of organic compounds emitted into the atmosphere primarily by vegetation, including trees, shrubs, and other plants. BVOCs react rapidly with atmospheric oxidants, such as hydroxyl radicals (OH), ozone (O_3), and nitrate radicals (NO_3), leading to changes in tropospheric ozone levels, but also producing a range of oxidation products that contribute to the formation of secondary organic aerosols (SOAs).[1–4] The produced biogenic

[a]Institute of Chemical Engineering Sciences, ICE-HT, 26504, Patras, Greece
[b]Department of Chemical Engineering, Carnegie Mellon University, Pittsburgh, PA 15213, USA
[c]Institute of Physical Chemistry, Polish Academy of Sciences, 01-224 Warsaw, Poland
[d]Department of Chemical Engineering, University of Patras, 26504 Patras, Greece. E-mail: spyros@chemeng.upatras.gr
† Present address: TOFWERK, 3645 Thun, Switzerland.

© 2026 The Author(s). Published by the Royal Society of Chemistry

Open Access Article. Published on 08 November 2025. Downloaded on 2/14/2026 3:37:43 AM.
This article is licensed under a Creative Commons Attribution 3.0 Unported Licence.

SOA is often the most significant component of OA in the atmosphere, influencing the global radiative balance and affecting local and regional air quality. The role of bVOCs in OA formation has garnered considerable attention, as their emissions globally surpass anthropogenic emissions.[5,6]

Isoprene, monoterpenes, and sesquiterpenes account for roughly 75% of total global bVOC emissions,[6,7] while in certain summer periods their contribution can increase to over 90%.[8] Monoterpenes ($C_{10}H_{16}$) are significant bVOCs (11–15%),[7,9,10] particularly in forested regions. Although monoterpenes are emitted in lower quantities compared to isoprene, their potential to form SOA is considerably higher, accounting in certain cases for nearly half of the total fine OA in the atmosphere.[11]

α-Pinene and β-pinene are the most abundant monoterpenes, with global emissions ranging between 30 and 70 TgC annually.[7] Oxidation reactions of α-pinene and β-pinene generate a range of secondary products, with diaterpenylic acid acetate (DTAA) being one of them (Fig. 1). The oxidation process of α-pinene comprises several steps, beginning with the formation of peroxy radicals, followed by reactions that yield terpenylic acid and diaterpenylic acid. Terpenylic acid is mainly formed from the α- and β-pinene ozonolysis and from the photo-oxidation of nopinone during the aging of β-pinene first-generation products.[12–14] Mutzel *et al.* (2016)[14] suggested that the oxidation of myrtenal, an α-pinene SOA product, also leads to the formation of terpenylic acid. Yasmeen *et al.* (2010)[15] suggested that terpenylic acid can then undergo acid-catalyzed hydrolysis, resulting in the formation of diaterpenylic acid, a hydroxy-carboxylic acid. Diaterpenylic acid can subsequently undergo acetylation to produce DTAA ($C_{10}H_{16}O_6$; *m*/*z* 232). DTAA can also be produced through the oxidation of 1,8-cineole (eucalyptol), a naturally occurring cyclic ether derived from botanical sources such as eucalyptus, rosemary, and camphor laurel. According to Iinuma *et al.* (2009),[16] this formation occurs under both low and high NO_x conditions (Fig. 1).

Several studies have measured the levels of DTAA in various ambient environments, providing insights into its spatial and temporal distribution. DTAA has been detected in aerosol samples from forested areas with significant monoterpene emissions. Gómez-González *et al.* (2012)[17] reported ambient concentrations of DTAA ranging from 0.10 to 0.64 ng m^{-3} during the summer of 2007 at a forest site in Brasschaat, Belgium. Similarly, measurements in the spring of 2008 at a coniferous forest near Silkeborg, Denmark, recorded an average DTAA concentration of 0.4 ng m^{-3}, with peak values reaching 1.4 ng m^{-3}.[18] At a ponderosa pine plantation in the Sierra Nevada Mountains, California, DTAA concentrations were 5 ng m^{-3} during measurements conducted at the cold period of 2007, increasing to 6.5 ng m^{-3} during a warmer period in 2009.[19] At a rural background station in Vavihill, Sweden, characterized by a mix of pastures, forests, and agricultural land, Martinsson *et al.* (2017)[20] observed a mean DTAA concentration of 0.84 ng m^{-3}. Amarandei *et al.* (2023)[21] recorded average DTAA values ranging from 0.6 ng m^{-3} during the colder months to 1.7 ng m^{-3} in the warmer months in an urban site in Iasi, Romania. At a marine site surrounded by grasslands (Cape Grim, Australia), Cui *et al.*[22] (2019) measured a mean DTAA concentration of 0.11 ng m^{-3}, with peak values of up to 0.36 ng m^{-3}. Over a 24-year period, DTAA has been found to be the most abundant monoterpene-derived SOA component in Cape Grim, followed by terpenylic acid, terebic acid, MBTCA, and pinic acid.[22] Research conducted at Zeppelin Mountain (Svalbard) and Station Nord (Greenland) showed that DTAA was present in considerable amounts, particularly during periods of Arctic haze.[23] Hansen *et al.*[23] (2014) reported DTAA concentrations of 0.03–0.16 ng m^{-3} at Zeppelin Mountain and 0.01–0.05 ng m^{-3} at Station Nord during these events. These findings contribute valuable data on the role of DTAA in SOA formation across diverse environments.

Even though DTAA has been detected in various field campaigns, there are limited studies about its physicochemical properties.[24] DTAA is expected to react with hydroxyl (OH) radicals, though its subsequent reaction pathways remain unclear. These reactions may yield more oxidized products or result in fragmentation into smaller, volatile products. A deeper understanding of these oxidation processes for DTAA and other

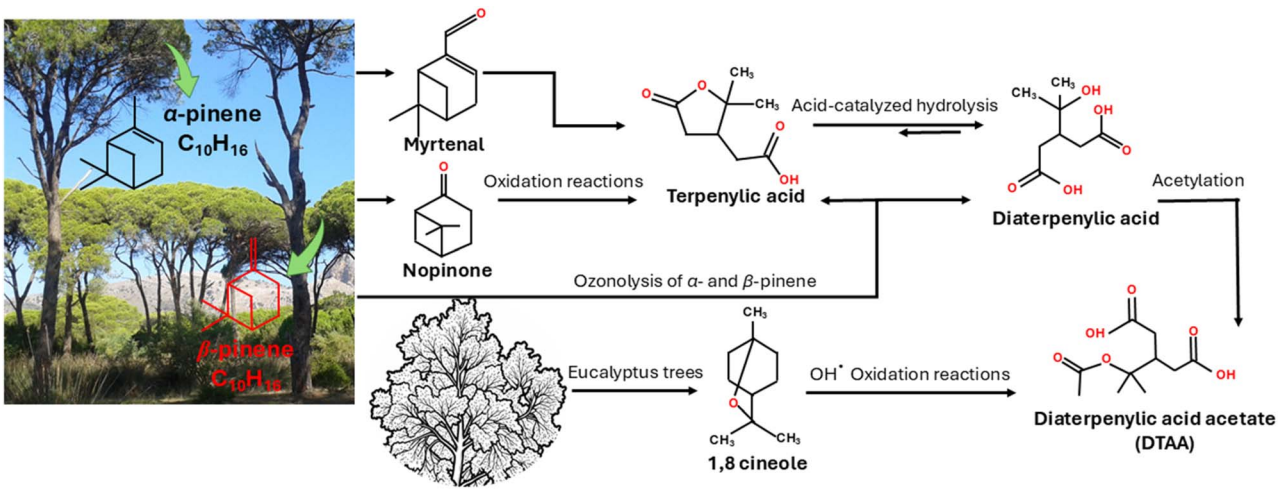

Fig. 1 Simplified schematic representation of the reaction pathways leading to the formation of DTAA.

Open Access Article. Published on 08 November 2025. Downloaded on 2/14/2026 3:37:43 AM. This article is licensed under a Creative Commons Attribution 3.0 Unported Licence.

similar SOA compounds is essential for enhancing atmospheric chemical transport models and better constraining the contribution of biogenic SOA to total OA.

In this study, we employed two distinct atmospheric simulation chambers in conjunction with advanced online instrumentation to characterize the physicochemical properties of aerosol composed of pure DTAA. Using high-resolution mass spectrometry, we characterized the aerosol's OA spectrum and determined key physicochemical parameters, including density, saturation vapor concentration, and enthalpy of vaporization. Furthermore, we investigated the chemical aging processes of DTAA by examining its reaction with hydroxyl radicals, under low- and high-NO_x conditions, followed by a detailed particle and gas phase analysis of the resulting oxidation products.

2 Experimental approach and methods

The synthesis of diaterpenylic acid acetate (DTAA) took place at the Institute of Physical Chemistry in Warsaw (Poland) and involved three main steps.[24] The first step is a Grignard reaction, where a solution of methylmagnesium bromide is added to methyl cyclopent-3-ene-1-carboxylate under anhydrous conditions, resulting in the formation of a tertiary alcohol. In the second step, this alcohol undergoes acylation using acetic anhydride, triethylamine, and 4-dimethylaminopyridine (DMAP), producing an acetate derivative. Finally, the third step involves oxidative cleavage of the carbon–carbon bond in the acetate using ruthenium trichloride and sodium periodate. DTAA was isolated as white crystals with a yield of 83% following recrystallization from a methylene chloride/pentane solution. A detailed description of the synthesis of DTAA can be found in the work of Kołodziejczyk *et al.* (2020).[24]

Aerosol samples were generated by atomizing an aqueous solution of DTAA. For selected experiments, ammonium sulfate was added to the solution to create mixed DTAA-ammonium sulfate particles. These aerosols were introduced into two atmospheric simulation chambers: the Foundation of Research and Technology-Hellas Atmospheric Simulation Chamber (FORTH-ASC) in Patras, Greece, and the Carnegie Mellon University Atmospheric Simulation Chamber (CMU-ASC) in Pittsburgh, USA. Initial characterization of the aerosol was conducted under dark conditions. Subsequently, atmospherically relevant levels of OH radicals were generated and allowed to react with DTAA.

Both chambers utilized a 10 m^3 Teflon reactor for the experiments. In the FORTH-ASC, the chamber walls were equipped with ultraviolet (UV) lamps (Osram, L 36W/73), achieving a J_{NO_2} of 0.59 min^{-1} when fully illuminated. The CMU-ASC featured similar UV lamps, resulting in a J_{NO_2} of 0.2 min^{-1}. Using two different chambers enhanced the robustness of the results, ensuring that potential wall-related artifacts were accounted for. Relative humidity (RH) in the chambers was maintained between 10% and 30%.

A constant output TSI atomizer (model 3076) was employed to produce aerosols from the prepared aqueous solutions. Experiments were conducted either in the absence of an aerosol seed or using ammonium sulfate seeds. In cases where the aerosol contained both DTAA and ammonium sulfate, the aerosol was generated from a single solution and introduced into the chamber. Prior to entering the chamber, the aerosol droplets were dried using a diffusion dryer.

Oxidation experiments were performed under low- and high-NO_x conditions. Under low-NO_x conditions, hydrogen peroxide (H_2O_2) photolysis served as the source of OH radicals, whereas in high-NO_x experiments, OH was generated through the photolysis of nitrous acid (HONO). Aqueous HONO was prepared by mixing fresh sulfuric acid (H_2SO_4) (4.9 g L^{-1}) with sodium nitrite ($NaNO_2$) (6.9 g L^{-1}) in a glass bulb, and HONO was introduced into the chamber using dry zero air and a bubbler. In specific experiments, isotopically labelled butanol d-9 (98%, Cambridge Isotope Laboratories, Inc.) was used to quantify OH levels. The chambers were thoroughly cleaned by flushing with clean air overnight prior to each experiment.

Initial concentrations of DTAA aerosol are shown in Table 1. DTAA was examined using two systems: (i) ammonium sulfate seed particles mixed with DTAA, forming internally mixed particles, and (ii) pure DTAA (*e.g.* Exp. 7). This dual approach was chosen to both assess the impact of impurities and also to isolate the behavior and oxidation chemistry of DTAA while

Table 1 Experimental parameters for the experiments conducted in the FORTH and CMU chambers during the characterization period

	Experimental conditions				Initial conditions					
Exp.	Type	Chamber	RH [%]	T [°C]	OA [μg m^{-3}]	Sulfate [μg m^{-3}]	Total PM_1 [μg m^{-3}]	O : C	H : C	OA density [g cm^{-3}]
1	Reference	FORTH	22	27	56	12	71	0.54	1.57	1.30
2	Reference	FORTH	18	25	29	7	39	0.57	1.64	1.29
3	HONO/UV	FORTH	10	24	34	9	47	0.55	1.64	1.28
4	HONO/UV	FORTH	14	25	25	37	78	0.57	1.63	1.30
5	HONO/UV	FORTH	31	19	59	14	79	0.53	1.58	1.29
6	H_2O_2/UV	FORTH	38	25	50	20	77	0.55	1.64	1.28
7	HONO/UV	FORTH	9	24	81	0	81	0.53	1.62	1.28
8	HONO/UV	CMU	10	21	24	10	37	0.55	1.53	1.32
9	HONO/UV	CMU	10	22	54	27	88	0.53	1.50	1.32
10	HONO/UV	CMU	14	20	41	33	85	0.56	1.51	1.34
Average values ± SD			17.6 ± 10.0	23.1 ± 2.6				0.55 ± 0.02	1.59 ± 0.06	1.30 ± 0.02

 © 2026 The Author(s). Published by the Royal Society of Chemistry

Open Access Article. Published on 08 November 2025. Downloaded on 2/14/2026 3:37:43 AM. This article is licensed under a Creative Commons Attribution 3.0 Unported Licence.

minimizing interference from other organic components. In the atmosphere, DTAA coexists with a complex mixture of organic species formed during monoterpene oxidation. Nevertheless, the simplified framework employed here provides essential insight into DTAA-specific processes and mechanisms, representing a necessary step toward understanding its behavior and role within more compositionally complex atmospheric environments. In our experiments, the equivalent ambient exposure of DTAA to OH varied from 0.6 to 0.9 days.

2.1 Instrumentation and methods

An Aerodyne High-Resolution Time-of-Flight Aerosol Mass Spectrometer (HR-ToF-AMS, Aerodyne Research Inc., Billerica, USA) was utilized in both experimental setups, sampling at a flow rate of approximately 0.1 L min^{-1}. This instrument provided continuous, real-time data on the size and chemical composition of non-refractory PM_1 aerosol particles (those with diameters less than 1 μm). Data from the HR-ToF-AMS were processed using standard AMS software toolkits: SeQUential Igor data RetRiEvaL (SQUIRREL) v1.57I and Peak Integration by Key Analysis (PIKA) v1.16I, within Igor Pro 6.37 (Wave Metrics). Elemental ratios, including the oxygen-to-carbon (O : C) ratio, were calculated using the enhanced method described by Canagaratna *et al.* (2015).[25]

The aerosol number distribution was measured using a TSI scanning mobility particle sizer (SMPS; classifier model 3080, DMA model 3081, CPC model 3787) over the size range of 14–710 nm every 3 min. The SMPS operated with a sheath flow rate of 3 L min^{-1} and an aerosol sample flow rate of 0.6 L min^{-1}. To characterize OA volatility, a thermodenuder[26] was employed. The thermodenuder was integrated with the SMPS and AMS to determine the aerosol mass fraction remaining (MFR) across temperatures ranging from 25 °C to 150 °C. Aerosol alternated between passing through the thermodenuder and a bypass line every 3 min, with both streams subsequently analyzed by the HR-AMS and SMPS. The aerosol had a centerline residence time of 15 s within the thermodenuder.

The dynamic mass transfer model developed by Riipinen *et al.* (2010)[27] was employed to estimate the volatility of OA. This model simulates the evaporation of particles within both the heating and cooling sections of the thermodenuder. Evaporation also occurs in the cooling section as organic vapors are removed by adsorption onto the activated carbon walls. The model estimates the mass fraction remaining (MFR), the OA saturation concentration (C^*) at 298 K and its effective vaporization enthalpy (ΔH_{vap}). For these simulations, the effective mass accommodation coefficient was assumed to be unity. The best estimates for C^* and ΔH_{vap} were derived from the top 1% of parameter combinations, which showed the lowest errors when comparing the measured MFR to model predictions.

Gas-phase compounds were monitored using a Proton Transfer Reaction Mass Spectrometer (PTR-MS 500, Ionicon Analytik), with H_3O^+ as the reagent ion. The PTR-MS operated at 600 V with a constant pressure of 2.2–2.3 mbar and a sampling flow rate of 0.5 L min^{-1}. Calibration was conducted according to the procedure outlined by Kaltsonoudis *et al.* (2016)[28] using VOC standards from Ionicon. The OH radical levels were determined based on the decay of butanol-d9, monitored at m/z 66 using the PTR-MS, and employing a reaction rate constant with OH of 3.4×10^{-12} cm^3 per molecule per s.[29]

DTAA reaction products were analyzed in the CMU-ASC using a time-of-flight chemical ionization mass spectrometer (ToF-CIMS, Aerodyne Research Inc.) with two reagent ions: iodide (I^-) and nitrate (NO_3^-), depending on the experimental setup. The NO_3^- reagent ion has been widely employed for studying the composition of highly oxidized organics in laboratory and ambient air studies.[30–32] It has been particularly effective for probing nitrogen-containing oxidized monoterpenes, as demonstrated by Draper *et al.* (2019).[33] NO_3^- clusters selectively with highly oxidized compounds containing at least two hydrogen bond donor sites, making it invaluable for identifying the formation of such products in oxidation experiments. In contrast, iodide (I^-) has been extensively used to detect oxidized organic compounds and inorganic nitrogen species.[34–37] The dual use of I^- and NO_3^- reagent ions offers complementary insights, enhancing the mechanistic understanding of oxidation processes by capturing a broader range of oxidized products.

To determine the AMS collection efficiency (CE) and the OA density, we utilized the algorithm developed by Kostenidou *et al.* (2007),[38] which involves comparing the volume distributions obtained from the SMPS with the mass distributions obtained from the AMS. For addressing particle wall losses in both chambers, we applied a size-dependent particle wall loss rate constant, using ammonium sulfate seeds, as recommended by Wang *et al.* (2018).[39] Ammonium sulfate particles were generated using the constant output TSI atomizer, dried, and then introduced into the chamber either before or after each experiment. The wall-loss rate constant, k_c, was consistent across all experiments, with a value of $k_c = 0.08 \pm 0.05$ h^{-1} in both the FORTH-ASC and CMU-ASC chambers.

To assess the variability in the OA and SOA mass spectra measured by the AMS across different experiments, we employed the theta angle (θ). The theta angle method treats the AMS OA spectra as n-dimensional vectors, where n represents the number of mass-to-charge ratios (m/z), and calculates the angle between these vectors in the n-dimensional space.[40] A theta angle of less than 10° denotes a high degree of similarity between the spectra, whereas angles exceeding 25° indicate significant differences between the examined spectra.

3 Results

3.1 Characterization of pure DTAA

The initial DTAA concentrations in the two chambers ranged from approximately 24 to 81 μg m^{-3} (Table 1). The use of elevated concentrations, substantially exceeding ambient levels, was intentional to facilitate the investigation of DTAA's oxidation chemistry and particle-phase processes in real time under controlled conditions. At ambient concentrations, these transformations would be extremely challenging to resolve in chamber experiments, mainly due to the influence of background interferences. By employing higher concentrations, the study was able to characterize DTAA's behaviour and gain

Open Access Article. Published on 08 November 2025. Downloaded on 2/14/2026 3:37:43 AM.
This article is licensed under a Creative Commons Attribution 3.0 Unported Licence.

insights into its volatility, partitioning, and chemical aging. Although the absolute concentrations used differ from those typically observed in the atmosphere, the reaction pathways and mechanistic trends identified are expected to remain valid. Therefore, the results provide a foundation for understanding DTAA's role under more realistic atmospheric conditions.

In most experiments, ammonium sulfate seeds were introduced with DTAA in the same solution, and during the characterization period, sulfate levels were observed to be up to 34 μg m^{-3}. In Exp. 7, only DTAA was injected into the chamber. Relative humidity (RH) remained low in all experiments, varying from 9% to 38%, while the average temperature was maintained at 23 ± 3 °C (Table 1).

3.1.1 High resolution AMS spectrum of pure DTAA. Variations between the individual experimental mass spectra and the average mass spectrum were minimal, with the corresponding angles (θ) varying between 1° and 10° (R^2 values ranging from 0.93 to 1) (Fig. S1). The average high-resolution AMS spectrum of DTAA from all experiments is presented in Fig. 2, while the corresponding unit resolution mass spectrum is provided in Fig. S2.

The HR spectrum of DTAA was characterized by oxygenated fragment ions (58%), with contribution from the $C_xH_yO^+$ family at 39.7% and the $C_xH_yO_z^+$ family at 18.5% (Fig. 2). Significant $C_xH_yO^+$ ions were detected at *m/z* 43 ($C_2H_3O^+$), 59 ($C_3H_7O^+$), 71 ($C_4H_7O^+$), 85 ($C_5H_9O^+$), 95 ($C_6H_7O^+$), 108 ($C_7H_8O^+$), 109 ($C_7H_9O^+$), and 157 ($C_{11}H_9O^+$). Major $C_xH_yO_z^+$ ions included those at *m/z* 45 ($CH_4O_2^+$), 60 ($C_2H_4O_2^+$), 86 ($C_4H_6O_2^+$), 101 ($C_5H_9O_2^+$), 114 ($C_5H_6O_3^+$), 126 ($C_7H_{10}O_2^+$), 127 ($C_7H_{11}O_2^+$), 139 ($C_7H_7O_3^+$), and 154 ($C_8H_{10}O_3^+$). The C_xH_y family contributed 38.4% to the total OA signal, and the main *m/z* peaks included 53 ($C_4H_5^+$), 65 ($C_5H_5^+$), 67 ($C_5H_7^+$), 68 ($C_5H_8^+$), 77 ($C_6H_5^+$), 79 ($C_6H_7^+$), 81 ($C_6H_9^+$), and 91 ($C_7H_7^+$). The average unit resolution OA mass spectra from all experiments, along with the standard deviation, are shown in Fig. S2. The HR spectrum of DTAA exhibits a distinct profile, largely due to the significant number of detected *m/z* values, particularly those above *m/z* 100.

The O : C ratio for DTAA ($C_{10}H_{16}O_6$) is 0.6, and its H : C ratio is 1.6. Following the method of Canagaratna *et al.* (2015),[25] the AMS O : C and H : C ratios were estimated to be 0.55 ± 0.02 and 1.59 ± 0.06, which are consistent with the expected values. The Van Krevelen diagram of the OA for all experiments is shown in Fig. S3.

Applying the algorithm of Kostenidou *et al.*[38] (2007), the AMS collection efficiency (CE) was estimated to be 0.8 ± 0.1 and the pure DTAA density was 1.35 ± 0.15 g cm^{-3}. This value is close to the density of 1.30 ± 0.02 g cm^{-3} that is predicted by the Kuwata *et al.* (2012)[41] parameterization based on the actual O : C and H : C values for DTAA.

3.1.2 Results of a typical characterization experiment. During the characterization phase, DTAA aerosol was introduced into the dark chamber without the presence of any oxidants. The results of Exp. 1 corrected for particle wall losses are displayed in Fig. 3. DTAA and ammonium sulfate aerosol were injected into the chamber two hours prior to the defined time zero. In the characterization experiments (Exp. 1 and 2), time zero refers to an hour after the injection of DTAA aerosol in the chamber to ensure equilibrium of the aerosol. For a total of 12 h, the aerosols remained undisturbed in the dark. After applying corrections for particle wall losses, no significant changes were detected in the mass concentrations of sulfate and ammonium. The DTAA concentration, however, decreased consistently at a rate of 0.4 μg m^{-3} h^{-1}, falling from 56.7 μg m^{-3} to 54 μg m^{-3} over a 7-h period (Fig. 3a).

The SMPS mass concentration also demonstrated a consistent decrease, mirroring the trend observed in the AMS data. The data of characterization Exp. 2 were consistent with those of Exp. 1 (Fig. S4). During the characterization period, the AMS OA spectrum showed minimal changes (θ < 3°), and the O : C ratio of DTAA remained practically constant (less than 2% change), which is consistent with the minimal variation observed in the high-resolution OA spectrum.

At t = 0 h, the OA-to-sulfate ratio was 4.8, but this value progressively declined, reaching 4.3 after 6 h. Given that sulfate is non-volatile at room temperature, this decrease indicates that

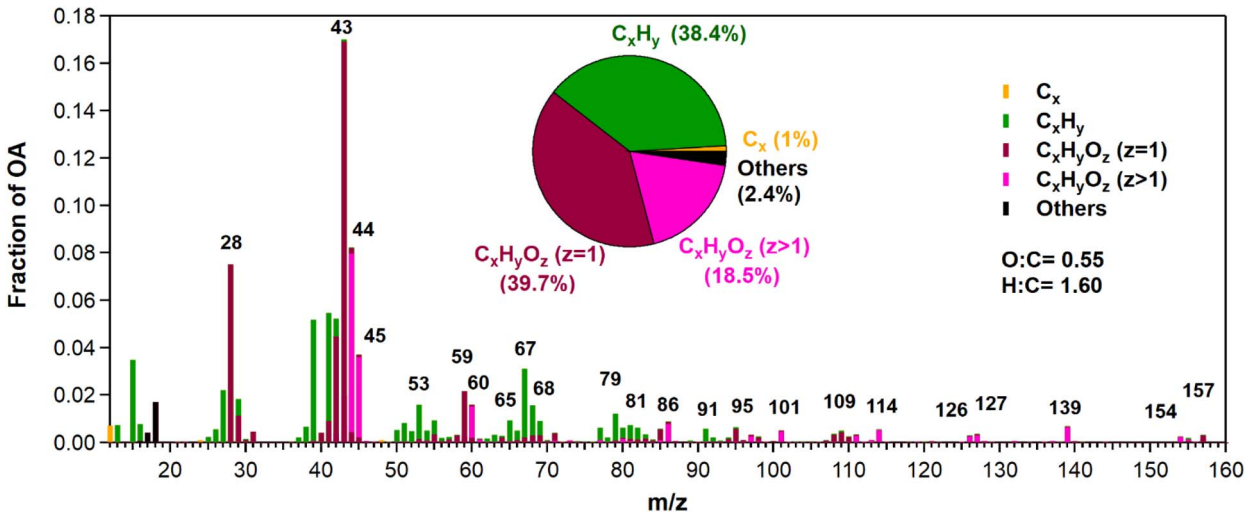

Fig. 2 HR average AMS spectrum of pure diaterpenylic acid acetate (DTAA) aerosol. The most important characteristic *m/z* ratios were 53, 59, 60, 65, 67, 68, 69, 71, 77, 79, 80, 81, 82, 85, 86, 91, 95, 101, 109, 114, 126, 127, 139, 154 and 157.

 © 2026 The Author(s). Published by the Royal Society of Chemistry

Open Access Article. Published on 08 November 2025. Downloaded on 2/14/2026 3:37:43 AM.
This article is licensed under a Creative Commons Attribution 3.0 Unported Licence.

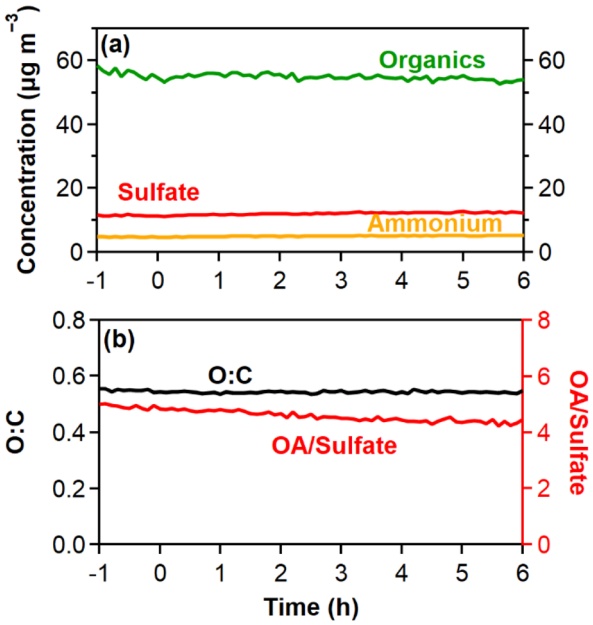

Fig. 3 The particle wall-loss corrected (a) mass concentration of OA, sulfate and ammonium in μg m^{-3} and (b) the O : C ratio (black line; left *y*-axis) and OA/sulfate ratio (red line; right *y*-axis) for Exp. 1.

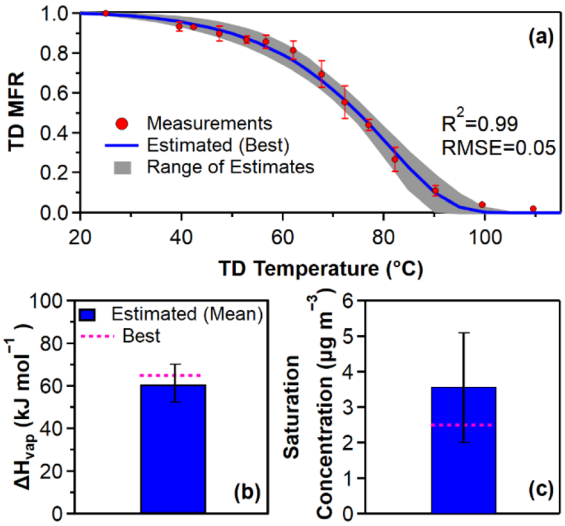

Fig. 4 (a) MFR after the TD for AMS measurements (red dots), the model average prediction (blue line), and the range of model estimates (grey area); (b) the mean estimated ΔH_{vap} (blue bar) and its best estimate (dashed pink line); and (c) the mean estimated C^* (blue bar) and its best estimate (dashed pink line). The measurements have been corrected for size- and temperature-dependent particle losses. The error bars correspond to one standard deviation.

DTAA gradually evaporated, with its vapor slowly depositing onto the chamber walls (Fig. 3b).

The observed reduction in OA concentration over time, coupled with the declining OA-to-sulfate ratio, provides evidence that DTAA, once introduced into the chamber, undergoes partial evaporation to establish equilibrium with the gas phase. The vapor wall loss rate will be estimated in a subsequent section.

3.1.3 Estimation of the volatility of pure DTAA. The mass fraction remaining (MFR) measured by the HR-ToF-AMS was calculated from the raw measurements after corrections for size- and temperature-dependent particle losses in the thermodenuder, as described by Louvaris *et al.* (2017).[42] The corrected AMS MFR for Exp. 1 is depicted in Fig. 4a. The data were grouped into bins of 5 °C up to 80 and 10 °C between 80 and 120 °C. Following the modeling approach described in Riipinen *et al.* (2010),[27] we used as inputs the corrected AMS MFR data and we estimated a saturation concentration of 3.6 ± 1.6 μg m^{-3} and a vaporization enthalpy of 61 ± 8 kJ mol^{-1} (Fig. 4b and c).

Kostenidou *et al.* (2022)[43] proposed a different method for calculating the saturation concentration at room temperature. This approach is based on the assumption that the difference between the initial OA concentration and its equilibrium concentration reflects the quantity that has evaporated into the gas phase, which corresponds to the saturation concentration. The proposed equation accounts for several factors, including the OA-to-sulfate ratio, the mass concentrations of OA and sulfate before evaporation, the final OA concentration, as well as adjustments for wall losses and deposition. Employing this methodology, the saturation concentration of DTAA was determined across all experiments during the characterization phase (defined as the 60 min prior to UV light activation in Experiments 3–10) to be 3.9 ± 3.6 μg m^{-3}. While this estimate carries greater uncertainty compared to values obtained from the thermodenuder analysis, both methods provide consistent results within the bounds of their experimental uncertainties. The value of this study is consistent considering the experimental uncertainties with the 1.7 μg m^{-3} measured by Babar *et al.* (2020).[44] As a result, DTAA can be classified as a semi-volatile organic compound (SVOC) based on these findings.

3.1.4 Losses of DTAA vapors to the chamber walls. Vapor wall losses can introduce a significant bias in atmospheric chamber studies, particularly in the quantification of semi-volatile organic compounds (SVOCs). Direct measurement of vapor wall loss rates for DTAA molecules is challenging. However, we can estimate these losses from the observed evaporation of DTAA particles in the characterization experiments and the estimated DTAA saturation concentration.

Assuming a linear loss process, the DTAA vapor wall loss rate constant $k_{wl,DTAA}$ can be estimated by:

$$k_{wl,DTAA} = \frac{\Delta C_{OA}}{C^* \Delta t} \quad (1)$$

where ΔC_{OA} is the change in particle wall-loss-corrected organic aerosol concentration in μg m^{-3} measured by the HR-ToF-AMS over the time period Δt, and C^* the estimated saturation concentration in μg m^{-3}. We are assuming that the DTAA particles are always in equilibrium with the vapor phase, and that the gas-phase DTAA concentration is constant and equal to its saturation concentration C^*.

Using this expression for the typical characterization experiment, we estimated a vapor wall loss rate of approximately 0.11 h^{-1}, with values ranging from 0.07 to 0.2 h^{-1}, depending on the C^* value. These values suggest slow but non-negligible

Open Access Article. Published on 08 November 2025. Downloaded on 2/14/2026 3:37:43 AM.
This article is licensed under a Creative Commons Attribution 3.0 Unported Licence.

removal of DTAA vapors to the chamber walls and will be used in our model in a subsequent section.

3.2 Chemical oxidation of DTAA

3.2.1 Particle phase: HR-ToF-AMS results. Approximately half an hour before the UV lights were turned on, HONO was introduced into the chamber for seven of the experiments (Table 1), while in Exp. 6, H_2O_2 was the source of OH. The equivalent OH exposure varied from 0.67 days in experiment 6 to 0.9 days in experiment 3, assuming a daily average OH concentration equal to 1.5×10^6 molecule per cm^3.[45] Time zero for all oxidation experiments was defined as the moment when the UV lights were turned on.

The O : C ratio for all oxidation experiments is displayed in Fig. 5. At time zero, the average O : C ratio for both the FORTH-ASC and CMU-ASC experiments was 0.55 ± 0.02 (Table 1). Following illumination, the O : C ratio remained relatively stable across all experiments, except for Experiment 5, where it decreased by 0.07 units to 0.48 after 6 h. The primary distinction of Exp. 5 is that it occurred predominantly at a significantly higher temperature than the other experiments (Fig. S6). Analysis of the AMS OA spectra revealed a change in the theta angle for the total OA spectrum of up to 8 degrees (Fig. 5b). The pre- and post-oxidation OA spectra exhibited noticeable differences across several *m*/*z* values, supporting the observed variation in the theta angle (Fig. S5).

The DTAA reaction with OH resulted in changes in the OA mass concentration in all oxidation experiments. The normalized change in OA concentration relative to the initial OA is illustrated in Fig. 6a. An enhancement of approximately 10% was observed in certain experiments (*e.g.*, Exp. 3 and 4), while others exhibited a moderate (5–16%) decrease (*e.g.*, Exp. 6, 7, and 8). In Experiments 5 and 10, there was a substantial reduction (35–60%) in OA. In Experiments 5 and 10, the observed OA reduction occurred at a much faster rate than the estimated DTAA vapor wall loss rate of 0.4 μg m^{-3} h^{-1}. For instance, in Experiment 5, the particle wall-loss-corrected OA concentration decreased by 21 μg m^{-3} over 6 hours, while vapor wall losses accounted for only 2.5 μg m^{-3} (12%) of this reduction. This pronounced decrease was primarily driven by enhanced evaporation caused by a 15 °C temperature increase in the chamber and the consequent acceleration of gas-phase oxidation processes. The relative contributions of these two effects can be estimated based on the experimental data. If

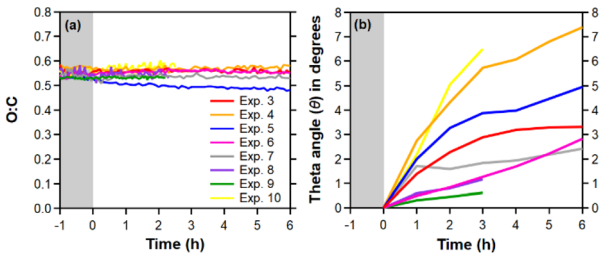

Fig. 5 The (a) O : C ratio for the aging experiments and (b) theta (*θ*) angles of the HR OA spectra for Experiments 3–10.

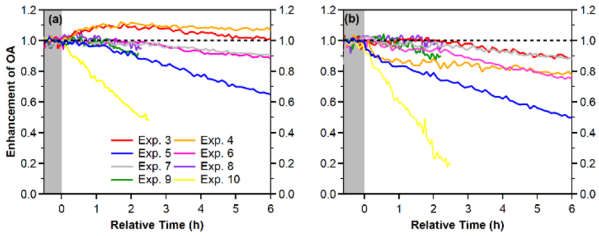

Fig. 6 Normalized change of (a) total OA and (b) pure DTAA (after applying PMF analysis) for the oxidation experiments once compared to initial conditions (time = 0).

evaporation alone were occurring, the OA loss would correspond to the change in saturation concentration over the 15 °C temperature range, amounting to approximately 5.3 μg m^{-3}. This value was derived from the reported saturation concentration at 298 K and the effective enthalpy of evaporation. Accounting for the estimated vapor wall loss (2.5 μg m^{-3}) and comparing with the total observed decrease in particulate-phase DTAA concentration (21 μg m^{-3}) indicates that most of the reduction was due to the gas-phase reactions.

Ammonium and sulfate mass concentrations remained stable in all experiments after applying the particle wall loss corrections, indicating that the corrections to AMS measurements, based on the corresponding wall loss characterization experiments, were reliable (Table 2).

A slight temperature increase of 2 °C, coinciding with the activation of UV lights, was observed in all oxidation experiments, with the exception of Experiment 5. In that case, a more pronounced temperature increase of 15 °C was recorded during the experiment because the chamber cooling system was deactivated (Fig. S6). This significant temperature increase may help explain the faster reduction in OA observed in Experiments 5 and 10, compared to the other experiments.

3.2.2 PMF analysis of OA. PMF analysis[46,47] was employed to deconvolute the HR-ToF-AMS organic mass spectra into fresh and aged DTAA aerosol. Solutions with one to five factors were examined, and the optimal configuration was determined based on several criteria, including the comparison of the factor profiles and their physical interpretability, the coherence and distinctness of the resulting time series, and the assessment of the model residuals. A marked decrease in Q/Q_{exp} was observed from one to two factors (1.5 at two factors), with only minor improvements for higher numbers of factors (1.35 at five factors). The three- and four-factor solutions produced noisier time series and highly similar mass spectra, suggesting factor splitting rather than distinct components. Since residuals beyond two factors showed negligible improvement, the two-factor solution was selected across all ten experiments as the most physically meaningful one.

The first factor corresponded to the HR spectrum of fresh DTAA (Fig. 2), measured in the characterization phase, with an AMS O : C ratio of 0.55. As chemical aging commenced, the mass concentration of the fresh DTAA factor decreased (Fig. 7), albeit at different rates in each experiment (Fig. 6b). The second factor was attributed to aged DTAA aerosol, hereafter referred to

 © 2026 The Author(s). Published by the Royal Society of Chemistry

Open Access Article. Published on 08 November 2025. Downloaded on 2/14/2026 3:37:43 AM.
This article is licensed under a Creative Commons Attribution 3.0 Unported Licence.

Table 2 Experimental parameters for $t = 3$ h for the 10 experiments

	Experimental parameters at $t = 3$ h					
Exp.	OA [μg m^{-3}]	Sulfate [μg m^{-3}]	Total PM$_1$ [μg m^{-3}]	O : C	H : C	OA density [g cm^{-3}]
1	55	12	70	0.54	1.57	1.30
2	26	7	35	0.57	1.64	1.30
3	37	9	49	0.56	1.64	1.29
4	28	37	80	0.57	1.62	1.30
5	50	14	69	0.49	1.61	1.26
6	49	20	76	0.56	1.64	1.29
7	79	0	79	0.54	1.64	1.28
8	23	10	37	0.53	1.53	1.31
9	49	27	85	0.53	1.50	1.32
10	18	32	62	0.58	1.41	1.38
Average values ± SD				0.55 ± 0.03	1.58 ± 0.08	1.30 ± 0.03

as SOA. SOA had practically zero mass concentration when the UV lights were off and increased once the aerosol was exposed to OH radicals and UV irradiation (Fig. 7). The SOA had an O : C ratio of 0.63 (Fig. 8), that is 0.08 units (15%) higher than the fresh DTAA. The SOA AMS spectrum differed significantly from the fresh DTAA spectrum, particularly at m/z 28, 29, 43, 44, 45, 55, 60, 61, 65, 67, 68, 79, 86, 101, 114, 139 and 157 (Fig. S7). Contributions from the $C_xH_yO^+$ and $C_xH_yO_z^+$ families to the SOA spectrum were 41.1% and 16.8%, respectively. The theta angle between the fresh DTAA and SOA factors was 31 degrees, indicating a substantial chemical transformation during aging.

The pure DTAA and PMF SOA HR spectra were compared with other biogenic-related and ambient factors reported in the literature (Table 3). The pure DTAA spectrum demonstrated a small similarity ($\theta = 22°$) to SOA formed from β-caryophyllene aging under high NO_x conditions.[48] Other compared spectra exhibited theta angles ranging from 23° to 46°, while the ambient biogenic factors had theta angles exceeding 32°. In contrast, the SOA factor showed a closer resemblance (theta angle of 14°) to SOA spectra resulting from α-pinene oxidation under high NO_x conditions, and around 20° when compared to the biogenic OA factors from two different locations in Greece (Pertouli and Patras).[49,50] This suggests a degree of similarity, though also noticeable differences between this SOA factor and the ambient field factors examined.

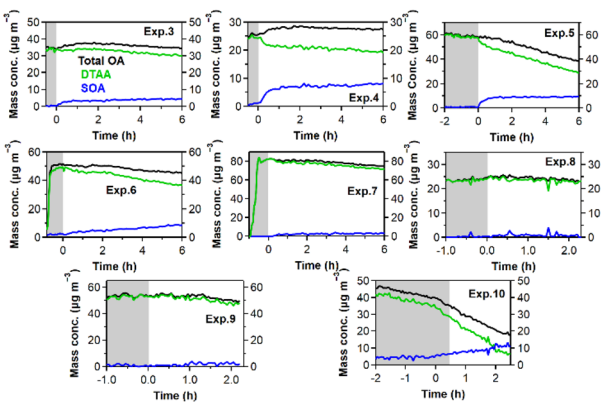

Fig. 7 Time series for total measured OA (dark green line), sulfate (red line), ammonium (orange line) and PMF OA factors for pure DTAA (light green line) and SOA (black line) for Experiments 3–10.

3.2.3 Gas-phase: CIMS and PTR-MS data. Complementary gas-phase measurements obtained using the ToF-CIMS during Experiment 8 at CMU are presented in Fig. 9. The signals for DTAA and other detected ions were normalized to the sum of the iodide reagent ion (I^-) and water clusters. Upon the injection of DTAA into the chamber, the CIMS immediately recorded an increase in its gas-phase concentration. Following exposure to OH radicals, there was a notable rise in the signals corresponding to $C_8H_{15}O_2I^-$ and, to a lesser extent, $C_8H_{11}O_4I^-$, both of which correspond to oxidation products with lower molecular weight than DTAA. Additional ions, including $C_6H_7O_2I^-$, and those at m/z 205.8, 222 and 261.96, also showed increased signals. However, it should be noted that the iodide-based CIMS may have limited efficiency in detecting larger oxidized molecules. To complement the findings from the iodide CIMS analysis, the NO_3^- CIMS was employed in Experiment 10, as shown in Fig. S8. Following the injection of DTAA into the chamber, a consistent increase in its signal was observed. After time zero, $C_7H_{10}O_4$ exhibited the most significant rise in signal, followed by $C_8H_{13}O_7$, indicating that both are prominent oxidation products. Additional species, including $C_3H_4O_3$, $C_4H_{10}O_9$, $C_{10}H_{16}O_3$, and signal at m/z 357, also showed notable increases. These observations highlight the diversity of oxidation products formed in the chamber and suggest the formation of both fragments and multifunctional compounds.

The PTR-MS detected increases in several VOCs across all FORTH-ASC experiments, including m/z 57 (butenes), 59 (acetone), 73 (methyl ethyl ketone), 81 (monoterpene fragment), 92 (unidentified), 93 (nominally toluene but also a monoterpene fragment), 95 (nominally phenol but also a monoterpene fragment), 103 (unidentified), 113 (biogenic oxidation product) and 115 (2-heptanone). The most significant increases were observed for m/z 57 (81 ± 31%), 81 (77 ± 37%) and 93 (77 ± 48%), which are commonly identified as monoterpene fragments when H_3O^+ is used as the reagent ion.[55,56] The signal at m/z 92 (increase of 45 ± 21%), previously linked to monoterpene

Open Access Article. Published on 08 November 2025. Downloaded on 2/14/2026 3:37:43 AM.
This article is licensed under a Creative Commons Attribution 3.0 Unported Licence.

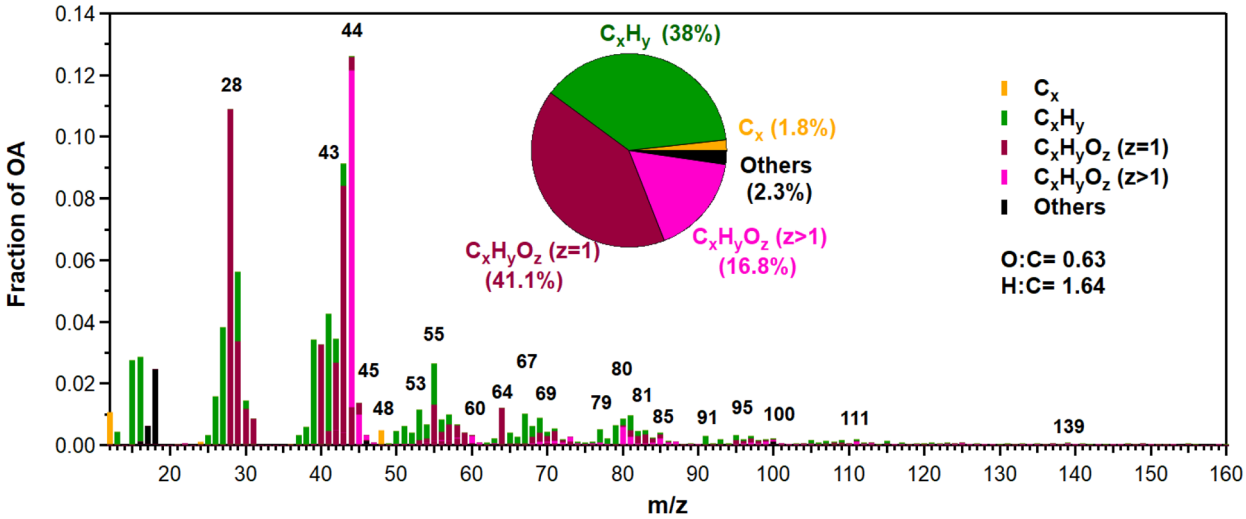

Fig. 8 HR mass spectrum of the SOA factor. The most important characteristic *m/z* ratios were 44, 45, 48, 53, 55, 64, 67, 69, 77, 79, 80, 81, 82, 85, 91, 95, 100, and 111.

oxidation products in similar studies using H_3O^+, also showed a consistent increase.[56] No increase of *m/z* 137 (monoterpenes) was detected. Quantitatively, *m/z* 59 (acetone) exhibited the highest enhancement, as high as 40 ppb, for the case of Experiment 5 (Fig. S9). To ensure this increase was due to the DTAA reactions rather than contamination from chamber walls, three blank experiments were conducted. The chamber was flushed overnight with clean air to ensure thorough cleaning before HONO was injected. UV lights were then activated, and the chamber was monitored for 3 h. In these blank experiments, an average acetone increase of 7 ppb was measured, verifying that the pronounced increase in *m/z* 59 was mainly due to the oxidation of DTAA. The acetone production observed is consistent with previous studies on α-pinene oxidation by ozone, OH and nitrate radicals, further supporting its attribution to DTAA oxidation processes.[57]

In order to examine the VOC oxidation products under relevant atmospheric conditions, the Generator for Explicit Chemistry and Kinetics of Organics in the Atmosphere (GECKO-A) (https://geckoa.lisa.u-pec.fr/) chemical mechanism was used to simulate the gaseous oxidation of DTAA.[58,59] GECKO-A automatically assigns reactions and rate constants and produces

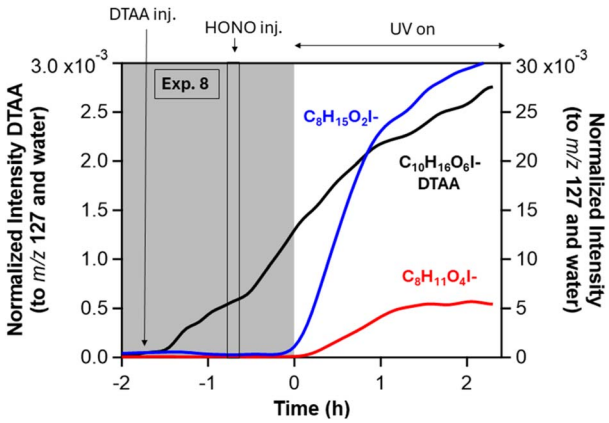

Fig. 9 CIMS time-series of DTAA (left *y*-axis) and products (right *y*-axis) for Exp. 8.

Table 3 Comparison between the pure DTAA and SOA PMF spectra to reference mass spectra

Factor from literature *vs.* DTAA	θ (°)	Factor from literature *vs.* SOA	θ (°)
SOA: β-caryophyllene + OH (high NO_x)[48]	22.2	SOA: α-pinene + OH (unpublished data)	14.2
SOA: limonene + OH (unpublished data)	23.1	Biogenic OA (Patras)[49]	18.6
α-Humelene initial (30–60 min)[51]	23.7	Biogenic OA (Pertouli)[50]	20.8
SOA: α-pinene + OH (unpublished data)	25.2	Terebic acid[52]	20.8
SOA: β-caryophyllene + O_3 (ref. 48)	26.5	SOA: β-caryophyllene + O_3 (ref. 48)	23.1
α-Humelene final (4–5 h)[51]	26.9	SOA: limonene + OH (unpublished data)	23.9
Terebic acid[52]	29.1	LO-OOA (Pertouli)[50]	24.1
SOA: β-caryophyllene + OH (low NO_x)[48]	30.5	SOA: β-caryophyllene + OH (high NO_x)[48]	25.1
Biogenic OA (Patras)[49]	32.5	α-Humelene initial (30–60 min)[51]	27.0
Biogenic OA (Pertouli)[50]	33.7	MBTCA[53]	27.6
LO-OOA (Pertouli)[50]	39.0	MO-OOA (Pertouli)[50]	27.9
Isoprene-OA (Centreville, Alabama)[54]	39.8	Isoprene-OA (Centreville, Alabama)[54]	28.0
MBTCA[53]	42.4	α-Humelene final (4–5 h)[51]	29.5
MO-OOA (Pertouli)[50]	43.0	Norpinic Acid[43]	34.1
Norpinic acid[43]	46.0	SOA: β-caryophyllene + OH (low NO_x)[48]	35.7

 © 2026 The Author(s). Published by the Royal Society of Chemistry

Open Access Article. Published on 08 November 2025. Downloaded on 2/14/2026 3:37:43 AM.
This article is licensed under a Creative Commons Attribution 3.0 Unported Licence.

detailed and explicit chemical mechanisms. The generated mechanism included 12 stable oxidation products (Fig. S10). The ToF-CIMS detected three of these 12 oxidation products (m/z 205.8, $C_3H_4O_3$ and $C_4H_{10}O_9$). The PTR-MS did not detect most of these products, mainly because the corresponding m/z ratios were not assigned. This discrepancy between the model-predicted and experimentally identified products could be partially due to limitations of the measurement techniques under the specific experimental conditions. Some predicted products may have been present at concentrations below the detection limits of CIMS and PTR-MS. In addition, highly functionalized species are more likely to be lost to chamber walls or sampling lines, further reducing their detectability. Finally, model predictions include possible products across a broad range of timescales and pathways, and some species may form too slowly to appear within the timeframe of our chamber experiments. As a result, the number of experimentally identified products likely underestimates the true overlap with model predictions.

According to GECKO-A, the reaction rate constant of DTAA with OH is 17×10^{-12} cm^3 per molecule per s.

3.2.4 Simulation of the DTAA reacting system. A mechanism was developed to simulate the previous experimental results. The model accounts for mass transfer between the gas and particle phases for both DTAA and its products, gas-phase reactions involving DTAA, and vapor wall losses of vapors of DTAA and its products. Key assumptions include: (a) DTAA and its products have similar molecular weights, (b) heterogeneous reactions are negligible, and (c) DTAA does not interact with preexisting inorganic aerosols.

The mechanism is described using the following set of equations:

$$\frac{dC_{g,DTAA}}{dt} = k_{mt,DTAA}\left(X_{p,DTAA}\, C^0_{DTAA} - C_{g,DTAA}\right) - k[OH]C_{g,DTAA} - k_{wl,DTAA}C_{g,DTAA} \quad (2)$$

$$\frac{dC_{p,DTAA}}{dt} = -k_{mt,DTAA}\left(X_{p,DTAA}C^0_{DTAA} - C_{g,DTAA}\right) \quad (3)$$

$$\frac{dC_{g,P}}{dt} = k_{mt,P}\left(X_{p,P}C^0_P - C_{g,P}\right) + \alpha k[OH]C_{g,DTAA} - k_{wl,P}C_{g,P} \quad (4)$$

$$\frac{dC_{p,P}}{dt} = -k_{mt,P}\left(X_{p,P}C^0_P - C_{g,P}\right) \quad (5)$$

where $C_{g,DTAA}$ and $C_{p,DTAA}$ are the concentrations of DTAA in the gas and particle phases, respectively, $C_{g,P}$ and $C_{p,P}$ are the concentrations of a surrogate species P representing its products in the gas and particle phases, $k_{mt,DTAA}$ and $k_{mt,P}$ are the mass transfer constants of DTAA and the product between the gas and particulate phases. The gas-phase reaction rate constant of DTAA is k. Vapor wall losses are represented by $k_{wl,DTAA}$ and $k_{wl,P}$ corresponding to DTAA and the product and are assumed to be equal to the DTAA measured value of 0.11 h^{-1}. C^0_{DTAA} and C^0_P denote the saturation concentrations of DTAA and the product, respectively. $X_{p,DTAA}$ and $X_{p,P}$ are the mass fractions of DTAA and the product in the particle phase. Finally, α represents the fraction of the DTAA products that are semivolatile and can form SOA. It can be viewed as an effective functionalization probability with $1 - \alpha$ representing the fragmentation probability. Due to the temperature variation observed during the experiments, the Clausius–Clapeyron equation was employed to account for the temperature dependence of vapor pressure in the model calculations.

The system of eqn (2)–(5) was solved using the following initial conditions:

$$C_{g,DTAA}\,(t = 0) = C^0_{DTAA} \quad (6)$$

$$C_{p,DTAA}\,(t = 0) = OA \quad (7)$$

$$C_{g,P}\,(t = 0) = 0 \quad (8)$$

$$C_{p,P}\,(t = 0) = 0 \quad (9)$$

and varying the parameter α from 0 to 1. For each case, the root mean squared error (RMSE) was calculated, with the minimum RMSE occurring for $\alpha = 0.68$.

Model results are compared to experimental data from three representative oxidation experiments—Experiment 6 (low-NO_x, FORTH-ASC), Experiment 7 (high-NO_x, no ammonium sulfate seeds, FORTH-ASC), and Experiment 9 (high-NO_x, CMU-ASC) in Fig. 10. Despite the differences in NO_x regimes, presence/absence of seeds and chamber setups, the simple model was able to capture the observed changes in pure DTAA and formed SOA in all cases. This consistency across diverse experimental conditions highlights the robustness and applicability of the proposed framework for describing DTAA behaviour under varying atmospheric scenarios. A fragmentation probability of

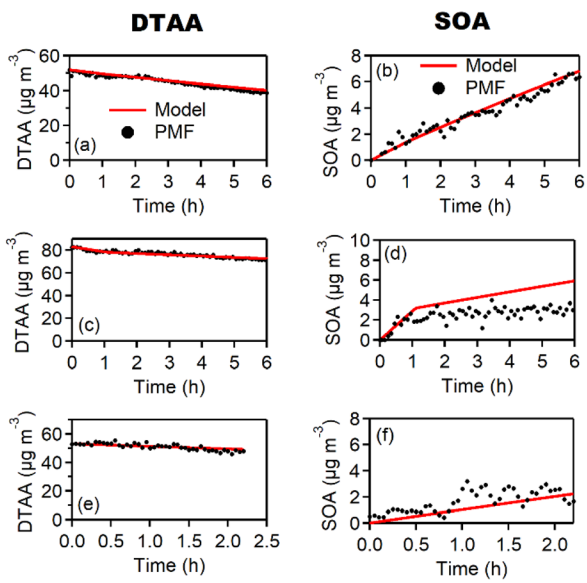

Fig. 10 Comparison of model predictions (red line) and experimental measurements (black dots) (in μg m^{-3}) for three representative oxidation experiments: (a and b) Experiment 6 (low-NO_x, FORTH-ASC), (c and d) Experiment 7 (high-NO_x, FORTH-ASC), and (e and f) Experiment 9 (high-NO_x, CMU-ASC). Panels show pure DTAA and secondary organic aerosol (SOA) formation over time.

Open Access Article. Published on 08 November 2025. Downloaded on 2/14/2026 3:37:43 AM. This article is licensed under a Creative Commons Attribution 3.0 Unported Licence.

0.32 appears to describe its reaction with OH. This probability denotes the fraction of the mass that is converted to high volatility products and therefore does not partition any more to the particle phase.

The model used in this study was designed to capture the dominant partitioning and fragmentation behaviour of DTAA under a range of conditions, and therefore it oversimplifies the gas-phase chemistry and neglects certain processes such as heterogeneous reactions, chamber-specific wall-loss variability, and detailed volatility distributions of the various products. These simplifications likely contribute to the deviations observed between modelled and measured SOA. Particle-phase functionalization or oligomerization could enhance SOA mass beyond model predictions, whereas uncertainties in fragmentation probabilities and product volatilities may also play a role. Sensitivity analyses indicate that increasing the fraction of lower-volatility products or incorporating a modest particle-phase uptake term improves agreement between model results and measurements. These findings suggest that heterogeneous processes and product volatility assumptions are plausible contributors to the observed discrepancies. Although a complete mechanistic reconciliation is beyond the scope of this study, it is acknowledged that a more complex modelling framework is needed to fully reproduce all experimental outcomes.

4 Conclusions

This study offers the first in-depth investigation of DTAA oxidation in atmospheric simulation chambers, building upon its early identification as a tracer of biogenic SOA in ambient air.[13] Through a coordinated experimental and modeling approach, we explore how this structurally simple, yet atmospherically relevant, compound evolves—from injection to oxidation—and what its behaviour reveals about broader processes governing SOA formation.

DTAA at 298 K has a saturation concentration equal to 3.6 μg m^{-3} and an effective vaporization enthalpy of 61 ± 8 kJ mol^{-1}. It is a semi-volatile organic compound, and its atmospheric lifetime due to the oxidation by OH in the gas phase is estimated to be of the order of 5 h. This makes it a rather poor choice as a tracer for monoterpene SOA and its use will only provide a lower limit of its contribution to total OA.

The oxidation of DTAA by OH led to later-generation SOA that had O : C 0.08 units (15%) higher than the parent compound. Its AMS spectrum, determined by applying PMF to the results of all experiments, was significantly different than that of DTAA and had some similarity to other biogenic SOA spectra, particularly those associated with α-pinene SOA produced under high-NO_x conditions. Depending on the conditions, the oxidation of DTAA can lead to small increases or significant decreases in the SOA concentration. The sign of the change does depend on temperature, with decreases appearing at higher temperatures.

Analysis of the gas-phase products of the DTAA oxidation using PTR-MS and CIMS revealed the formation of both smaller and multifunctional oxidation products. These gas-phase products covered a wide chemical range, from smaller compounds such as acetone to larger, highly oxidized molecules. An effective fragmentation probability of 32% was estimated using a simple model of the system. The model successfully reproduced key features of our experiments, including the extent and timescale of SOA formation, offering a quantitative tool for understanding DTAA's role in oxidative aerosol production.

The loss rate constant of DTAA vapor to the walls of the FORTH chamber was estimated to be 0.11 h^{-1} on average, with values ranging from 0.07 to 0.2 h^{-1}. The corresponding losses are non-negligible and should be taken into account in experiments that last several hours, especially if the DTAA concentrations in the particle phase are low.

Together, these results show that DTAA is a reactive SVOC that contributes to SOA formation, but also continues reacting, forming a variety of products, both smaller and larger. Its transformation under OH exposure resembles that of more extensively studied biogenic compounds, but its distinct spectrum adds to the chemical diversity of the ambient aerosol pool. The techniques used here can be used for other later-generation products of atmospheric VOC oxidation in an effort to improve our understanding of the later-generation processes taking place during atmospheric SOA formation.

Author contributions

K. F. and S. N. P. contributed to conceptualization; K. F., S. J., and A. B., contributed to investigation; K. F., S. J., A. B., C. V., P. U., R. S., and S. N. P. contributed to methodology, K. F., S. J., C. V., and P. U. contributed to formal analysis; K. F. wrote the original draft; all authors contributed to review and editing.

Conflicts of interest

The authors declare that there are no conflicts to declare.

Data availability

Data will be made available on request.

Supplementary information (SI): (1) theta angles for all experiments during the characterization period, (2) the average DTAA spectrum from all experiments along with their standard deviation, (3) the Van Krevelen diagram of DTAA for the 10 experiments, (4) the volume distributions for every hour and the time series of AMS and SMPS for characterization experiment 2, (5) the comparison of before- and after-UV spectra for the oxidation experiments, (6) the temperature and RH time series for the FORTH-ASC, (7) the comparison of AMS mass spectra for DTAA and SOA, (8) the CIMS time-series for experiment 10, (9) the PTRMS-compounds that increased after injecting OH radicals and started UV irradiation for experiment 5, and (10) the products of the DTAA oxidation by OH predicted by GECKO-A. See DOI: **https://doi.org/10.1039/d5ea00086f**.

 © 2026 The Author(s). Published by the Royal Society of Chemistry

Open Access Article. Published on 08 November 2025. Downloaded on 2/14/2026 3:37:43 AM.
This article is licensed under a Creative Commons Attribution 3.0 Unported Licence.

Acknowledgements

This work was supported by the Chemical Evolution of Gas-and Particulate-Phase Organic Pollutants in the Atmosphere (CHEVOPIN) funded by the Hellenic Foundation for Research & Innovation (HFRI) (grant agreement no. 1819) and the Atmospheric Nanoparticles, Air Quality and Human Health (NANOSOMs) project of HFRI (grant agreement no. 11504).

References

1 G. M. Wolfe, J. A. Thornton, M. McKay and A. H. Goldstein, Forest-atmosphere exchange of ozone: sensitivity to very reactive biogenic VOC emissions and implications for in-canopy photochemistry, *Atmos. Chem. Phys.*, 2011, **11**, 7875–7891.

2 K. Wu, X. Yang, D. Chen, S. Gu, Y. Lu, Q. Jiang, K. Wang, Y. Ou, Y. Qian, P. Shao and S. Lu, Estimation of biogenic VOC emissions and their corresponding impact on ozone and secondary organic aerosol formation in China, *Atmos. Res.*, 2020, **231**, 104656.

3 M. Hallquist, J. C. Wenger, U. Baltensperger, Y. Rudich, D. Simpson, M. Claeys, J. Dommen, N. M. Donahue, C. George, A. H. Goldstein, J. F. Hamilton, H. Herrmann, T. Hoffmann, Y. Iinuma, M. Jang, M. E. Jenkin, J. L. Jimenez, A. Kiendler-Scharr, W. Maenhaut, G. McFiggans, T. F. Mentel, A. Monod, A. S. H. Prévôt, J. H. Seinfeld, J. D. Surratt, R. Szmigielski and J. Wildt, The formation, properties and impact of secondary organic aerosol: current and emerging issues, *Atmos. Chem. Phys.*, 2009, **9**, 5155–5236.

4 P. Ciccioli, C. Silibello, S. Finardi, N. Pepe, P. Ciccioli, F. Rapparini, L. Neri, S. Fares, F. Brilli, M. Mircea, E. Magliulo and R. Baraldi, The potential impact of biogenic volatile organic compounds (BVOCs) from terrestrial vegetation on a Mediterranean area using two different emission models, *Agric. For. Meteorol.*, 2023, **328**, 109255.

5 A. Guenther, C. N. Hewitt, D. Erickson, R. Fall, C. Geron, T. Graedel, P. Harley, L. Klinger, M. Lerdau, W. A. Mckay, T. Pierce, B. Scholes, R. Steinbrecher, R. Tallamraju, J. Taylor and P. Zimmerman, A global model of natural volatile organic compound emissions, *J. Geophys. Res.:Atmos.*, 1995, **100**, 8873–8892.

6 A. B. Guenther, X. Jiang, C. L. Heald, T. Sakulyanontvittaya, T. Duhl, L. K. Emmons and X. Wang, The Model of Emissions of Gases and Aerosols from Nature version 2.1 (MEGAN2.1): an extended and updated framework for modeling biogenic emissions, *Geosci. Model Dev.*, 2012, **5**, 1471–1492.

7 K. Sindelarova, C. Granier, I. Bouarar, A. Guenther, S. Tilmes, T. Stavrakou, J.-F. Müller, U. Kuhn, P. Stefani and W. Knorr, Global data set of biogenic VOC emissions calculated by the MEGAN model over the last 30 years, *Atmos. Chem. Phys.*, 2014, **14**, 9317–9341.

8 J. Bai, A. Guenther, A. Turnipseed and T. Duhl, Seasonal and interannual variations in whole-ecosystem isoprene and monoterpene emissions from a temperate mixed forest in Northern China, *Atmos. Pollut. Res.*, 2015, **6**, 696–707.

9 J. Cao, S. Situ, Y. Hao, S. Xie and L. Li, Enhanced summertime ozone and SOA from biogenic volatile organic compound (BVOC) emissions due to vegetation biomass variability during 1981–2018 in China, *Atmos. Chem. Phys.*, 2022, **22**, 2351–2364.

10 Y. Fu and H. Liao, Simulation of the interannual variations of biogenic emissions of volatile organic compounds in China: Impacts on tropospheric ozone and secondary organic aerosol, *Atmos. Environ.*, 2012, **59**, 170–185.

11 H. Zhang, L. D. Yee, B. H. Lee, M. P. Curtis, D. R. Worton, G. Isaacman-VanWertz, J. H. Offenberg, M. Lewandowski, T. E. Kleindienst, M. R. Beaver, A. L. Holder, W. A. Lonneman, K. S. Docherty, M. Jaoui, H. O. T. Pye, W. Hu, D. A. Day, P. Campuzano-Jost, J. L. Jimenez, H. Guo, R. J. Weber, J. de Gouw, A. R. Koss, E. S. Edgerton, W. Brune, C. Mohr, F. D. Lopez-Hilfiker, A. Lutz, N. M. Kreisberg, S. R. Spielman, S. V. Hering, K. R. Wilson, J. A. Thornton and A. H. Goldstein, Monoterpenes are the largest source of summertime organic aerosol in the southeastern United States, *Proc. Natl. Acad. Sci. U. S. A.*, 2018, **115**, 2038–2043.

12 K. Sato, T. Jia, K. Tanabe, Y. Morino, Y. Kajii and T. Imamura, Terpenylic acid and nine-carbon multifunctional compounds formed during the aging of β-pinene ozonolysis secondary organic aerosol, *Atmos. Environ.*, 2016, **130**, 127–135.

13 M. Claeys, Y. Iinuma, R. Szmigielski, J. D. Surratt, F. Blockhuys, C. Van Alsenoy, O. Böge, B. Sierau, Y. Gómez-González, R. Vermeylen, P. Van der Veken, M. Shahgholi, A. W. H. Chan, H. Herrmann, J. H. Seinfeld and W. Maenhaut, Terpenylic acid and related compounds from the oxidation of α-pinene: Implications for new particle formation and growth above forests, *Environ. Sci. Technol.*, 2009, **43**, 6976–6982.

14 A. Mutzel, M. Rodigast, Y. Iinuma, O. Böge and H. Herrmann, Monoterpene SOA – Contribution of first-generation oxidation products to formation and chemical composition, *Atmos. Environ.*, 2016, **130**, 136–144.

15 F. Yasmeen, R. Vermeylen, R. Szmigielski, Y. Iinuma, O. Böge, H. Herrmann, W. Maenhaut and M. Claeys, Terpenylic acid and related compounds: precursors for dimers in secondary organic aerosol from the ozonolysis of α- and β-pinene, *Atmos. Chem. Phys.*, 2010, **10**, 9383–9392.

16 Y. Iinuma, M. Keywood, T. Gnauk and H. Herrmann, Diaterebic Acid Acetate and Diaterpenylic Acid Acetate: Atmospheric Tracers for Secondary Organic Aerosol Formation from 1,8-Cineole Oxidation, *Environ. Sci. Technol.*, 2009, **43**, 280–285.

17 Y. Gómez-González, W. Wang, R. Vermeylen, X. Chi, J. Neirynck, I. A. Janssens, W. Maenhaut and M. Claeys, Chemical characterisation of atmospheric aerosols during a 2007 summer field campaign at Brasschaat, Belgium: sources and source processes of biogenic secondary organic aerosol, *Atmos. Chem. Phys.*, 2012, **12**, 125–138.

Open Access Article. Published on 08 November 2025. Downloaded on 2/14/2026 3:37:43 AM.
This article is licensed under a Creative Commons Attribution 3.0 Unported Licence.

18 K. Kristensen and M. Glasius, Organosulfates and oxidation products from biogenic hydrocarbons in fine aerosols from a forest in North West Europe during spring, *Atmos. Environ.*, 2011, **45**, 4546–4556.

19 K. Kristensen, K. L. Enggrob, S. M. King, D. R. Worton, S. M. Platt, R. Mortensen, T. Rosenoern, J. D. Surratt, M. Bilde, A. H. Goldstein and M. Glasius, Formation and occurrence of dimer esters of pinene oxidation products in atmospheric aerosols, *Atmos. Chem. Phys.*, 2013, **13**, 3763–3776.

20 J. Martinsson, G. Monteil, M. K. Sporre, A. M. Kaldal Hansen, A. Kristensson, K. Eriksson Stenström, E. Swietlicki and M. Glasius, Exploring sources of biogenic secondary organic aerosol compounds using chemical analysis and the FLEXPART model, *Atmos. Chem. Phys.*, 2017, **17**, 11025–11040.

21 C. Amarandei, R. I. Olariu and C. Arsene, First insights into the molecular characteristics of atmospheric organic aerosols from Iasi, Romania: Behavior of biogenic versus anthropogenic contributions and potential implications, *Sci. Total Environ.*, 2023, **877**, 162830.

22 T. Cui, H. S. Green, P. W. Selleck, Z. Zhang, R. E. O'Brien, A. Gold, M. Keywood, J. H. Kroll and J. D. Surratt, Chemical Characterization of Isoprene- and Monoterpene-Derived Secondary Organic Aerosol Tracers in Remote Marine Aerosols over a Quarter Century, *ACS Earth Space Chem.*, 2019, **3**, 935–946.

23 A. M. K. Hansen, K. Kristensen, Q. T. Nguyen, A. Zare, F. Cozzi, J. K. Nøjgaard, H. Skov, J. Brandt, J. H. Christensen, J. Ström, P. Tunved, R. Krejci and M. Glasius, Organosulfates and organic acids in Arctic aerosols: speciation, annual variation and concentration levels, *Atmos. Chem. Phys.*, 2014, **14**, 7807–7823.

24 A. Kołodziejczyk, P. Pyrcz, K. Błaziak, A. Pobudkowska, K. Sarang and R. Szmigielski, Physicochemical properties of terebic acid, MBTCA, diaterpenylic acid acetate, and pinanediol as relevant α-pinene oxidation products, *ACS Omega*, 2020, **5**, 7919–7927.

25 M. R. Canagaratna, J. L. Jimenez, J. H. Kroll, Q. Chen, S. H. Kessler, P. Massoli, L. Hildebrandt Ruiz, E. Fortner, L. R. Williams, K. R. Wilson, J. D. Surratt, N. M. Donahue, J. T. Jayne and D. R. Worsnop, Elemental ratio measurements of organic compounds using aerosol mass spectrometry: characterization, improved calibration, and implications, *Atmos. Chem. Phys.*, 2015, **15**, 253–272.

26 W. J. An, R. K. Pathak, B.-H. Lee and S. N. Pandis, Aerosol volatility measurement using an improved thermodenuder: Application to secondary organic aerosol, *J. Aerosol Sci.*, 2007, **38**, 305–314.

27 I. Riipinen, J. R. Pierce, N. M. Donahue and S. N. Pandis, Equilibration time scales of organic aerosol inside thermodenuders: Evaporation kinetics versus thermodynamics, *Atmos. Environ.*, 2010, **44**, 597–607.

28 C. Kaltsonoudis, E. Kostenidou, K. Florou, M. Psichoudaki and S. N. Pandis, Temporal variability and sources of VOCs in urban areas of the eastern Mediterranean, *Atmos. Chem. Phys.*, 2016, **16**, 14825–14842.

29 P. Barmet, J. Dommen, P. F. DeCarlo, T. Tritscher, a. P. Praplan, S. M. Platt, a. S. H. Prévôt, N. M. Donahue and U. Baltensperger, OH clock determination by proton transfer reaction mass spectrometry at an environmental chamber, *Atmos. Meas. Tech.*, 2012, **5**, 647–656.

30 T. Berndt, S. Richters, R. Kaethner, J. Voigtländer, F. Stratmann, M. Sipilä, M. Kulmala and H. Herrmann, Gas-Phase Ozonolysis of Cycloalkenes: Formation of Highly Oxidized RO 2 Radicals and Their Reactions with NO, NO 2 , SO 2 , and Other RO 2 Radicals, *J. Phys. Chem. A*, 2015, **119**, 10336–10348.

31 M. P. Rissanen, T. Kurtén, M. Sipilä, J. A. Thornton, J. Kangasluoma, N. Sarnela, H. Junninen, S. Jørgensen, S. Schallhart, M. K. Kajos, R. Taipale, M. Springer, T. F. Mentel, T. Ruuskanen, T. Petäjä, D. R. Worsnop, H. G. Kjaergaard and M. Ehn, The Formation of Highly Oxidized Multifunctional Products in the Ozonolysis of Cyclohexene, *J. Am. Chem. Soc.*, 2014, **136**, 15596–15606.

32 M. Riva, P. Rantala, J. E. Krechmer, O. Peräkylä, Y. Zhang, L. Heikkinen, O. Garmash, C. Yan, M. Kulmala, D. Worsnop and M. Ehn, Evaluating the performance of five different chemical ionization techniques for detecting gaseous oxygenated organic species, *Atmos. Meas. Tech.*, 2019, **12**, 2403–2421.

33 D. C. Draper, N. Myllys, N. Hyttinen, K. H. Møller, H. G. Kjaergaard, J. L. Fry, J. N. Smith and T. Kurtén, Formation of Highly Oxidized Molecules from NO 3 Radical Initiated Oxidation of Δ-3-Carene: A Mechanistic Study, *ACS Earth Space Chem.*, 2019, **3**, 1460–1470.

34 B. H. Lee, F. D. Lopez-Hilfiker, C. Mohr, T. Kurtén, D. R. Worsnop and J. A. Thornton, An iodide-adduct high-resolution time-of-flight chemical-ionization mass spectrometer: application to atmospheric inorganic and organic compounds, *Environ. Sci. Technol.*, 2014, **48**, 6309–6317.

35 D. Aljawhary, A. K. Y. Lee and J. P. D. Abbatt, High-resolution chemical ionization mass spectrometry (ToF-CIMS): application to study SOA composition and processing, *Atmos. Meas. Tech.*, 2013, **6**, 3211–3224.

36 P. Brophy and D. K. Farmer, A switchable reagent ion high resolution time-of-flight chemical ionization mass spectrometer for real-time measurement of gas phase oxidized species: characterization from the 2013 southern oxidant and aerosol study, *Atmos. Meas. Tech.*, 2015, **8**, 2945–2959.

37 F. D. Lopez-Hilfiker, S. Iyer, C. Mohr, B. H. Lee, E. L. D'Ambro, T. Kurtén and J. A. Thornton, Constraining the sensitivity of iodide adduct chemical ionization mass spectrometry to multifunctional organic molecules using the collision limit and thermodynamic stability of iodide ion adducts, *Atmos. Meas. Tech.*, 2016, **9**, 1505–1512.

38 E. Kostenidou, R. K. Pathak and S. N. Pandis, An algorithm for the calculation of secondary organic aerosol density combining AMS and SMPS data, *Aerosol Sci. Technol.*, 2007, **41**, 1002–1010.

39 N. Wang, S. D. Jorga, J. R. Pierce, N. M. Donahue and S. N. Pandis, Particle wall-loss correction methods in smog

 © 2026 The Author(s). Published by the Royal Society of Chemistry

Open Access Article. Published on 08 November 2025. Downloaded on 2/14/2026 3:37:43 AM.
This article is licensed under a Creative Commons Attribution 3.0 Unported Licence.

chamber experiments, *Atmos. Meas. Tech.*, 2018, **11**, 6577–6588.

40 E. Kostenidou, B.-H. Lee, G. J. Engelhart, J. R. Pierce and S. N. Pandis, Mass spectra deconvolution of low, medium, and high volatility biogenic secondary organic aerosol, *Environ. Sci. Technol.*, 2009, **43**, 4884–4889.

41 M. Kuwata, S. R. Zorn and S. T. Martin, Using elemental ratios to predict the density of organic material composed of carbon, hydrogen, and oxygen, *Environ. Sci. Technol.*, 2012, **46**, 787–794.

42 E. E. Louvaris, K. Florou, E. Karnezi, D. K. Papanastasiou, G. I. Gkatzelis and S. N. Pandis, Volatility of source apportioned wintertime organic aerosol in the city of Athens, *Atmos. Environ.*, 2017, **158**, 138–147.

43 E. Kostenidou, S. Jorga, J. K. Kodros, K. Florou, A. Kołodziejczyk, R. Szmigielski and S. N. Pandis, Properties and atmospheric oxidation of norpinic acid aerosol, *Atmosphere*, 2022, **13**, 1481.

44 Z. Bin Babar, F. Ashraf, J.-H. Park, P. D. Quang Dao, C. S. Cho and H.-J. Lim, Exploring Volatility Properties of Discrete Secondary Organic Aerosol Constituents of α-Pinene and Polycyclic Aromatic Hydrocarbons, *ACS Earth Space Chem.*, 2020, **4**, 2299–2311.

45 B. A. Nault, P. Campuzano-Jost, D. A. Day, J. C. Schroder, B. Anderson, A. J. Beyersdorf, D. R. Blake, W. H. Brune, Y. Choi, C. A. Corr, J. A. De Gouw, J. Dibb, J. P. Digangi, G. S. Diskin, A. Fried, L. Gregory Huey, M. J. Kim, C. J. Knote, K. D. Lamb, T. Lee, T. Park, S. E. Pusede, E. Scheuer, K. L. Thornhill, J. H. Woo and J. L. Jimenez, Secondary organic aerosol production from local emissions dominates the organic aerosol budget over Seoul, South Korea, during KORUS-AQ, *Atmos. Chem. Phys.*, 2018, **18**, 17769–17800.

46 P. Paatero and U. Tapper, Positive matrix factorization: A non-negative factor model with optimal utilization of error estimates of data values, *Environmetrics*, 1994, **5**, 111–126.

47 I. M. Ulbrich, M. R. Canagaratna, Q. Zhang, D. R. Worsnop and J. L. Jimenez, Interpretation of organic components from Positive Matrix Factorization of aerosol mass spectrometric data, *Atmos. Chem. Phys.*, 2009, **9**, 2891–2918.

48 A. Tasoglou and S. N. Pandis, Formation and chemical aging of secondary organic aerosol during the β-caryophyllene oxidation, *Atmos. Chem. Phys.*, 2015, **15**, 6035–6046.

49 E. Kostenidou, K. Florou, C. Kaltsonoudis, M. Tsiflikiotou, S. Vratolis, K. Eleftheriadis and S. N. Pandis, Sources and chemical characterization of organic aerosol during the summer in the eastern Mediterranean, *Atmos. Chem. Phys.*, 2015, **15**, 11355–11371.

50 C. N. Vasilakopoulou, A. Matrali, K. Skyllakou, M. Georgopoulou, A. Aktypis, K. Florou, C. Kaltsonoudis, E. Siouti, E. Kostenidou, A. Błaziak, A. Nenes, S. Papagiannis, K. Eleftheriadis, D. Patoulias, I. Kioutsioukis and S. N. Pandis, Rapid transformation of wildfire emissions to harmful background aerosol, *npj Clim. Atmos. Sci.*, 2023, **6**, 218.

51 D. J. Sippial, P. Uruci, E. Kostenidou and S. N. Pandis, Formation of secondary organic aerosol during the dark-ozonolysis of α-humulene, *Environ. Sci.: Atmos.*, 2023, **3**, 1025–1033.

52 K. Florou, A. Błaziak, S. Jorga, P. Uruci, C. N. Vasilakopoulou, R. Szmigielski and S. N. Pandis, Properties and Atmospheric Oxidation of Terebic Acid Aerosol, *ACS Earth Space Chem.*, 2024, **8**, 2090–2100.

53 E. Kostenidou, E. Karnezi, A. Kolodziejczyk, R. Szmigielski and S. N. Pandis, Physical and Chemical Properties of 3-Methyl-1,2,3-butanetricarboxylic Acid (MBTCA) Aerosol, *Environ. Sci. Technol.*, 2018, **52**, 1150–1155.

54 E. Kostenidou, E. Karnezi, J. Hite, A. Bougiatioti, K. Cerully, L. Xu, N. Ng, A. Nenes and S. Pandis, Organic aerosol in the summertime southeastern United States: Components and their link to volatility distribution, oxidation state and hygroscopicity, *Atmos. Chem. Phys.*, 2018, **18**, 5799–5819.

55 P. K. Misztal, M. R. Heal, E. Nemitz and J. N. Cape, Development of PTR-MS selectivity for structural isomers: Monoterpenes as a case study, *Int. J. Mass Spectrom.*, 2012, **310**, 10–19.

56 D. Materić, M. Lanza, P. Sulzer, J. Herbig, D. Bruhn, V. Gauci, N. Mason and C. Turner, Selective reagent ion-time of flight-mass spectrometry study of six common monoterpenes, *Int. J. Mass Spectrom.*, 2017, **421**, 40–50.

57 V. Librando and G. Tringali, Atmospheric fate of OH initiated oxidation of terpenes. Reaction mechanism of α-pinene degradation and secondary organic aerosol formation, *J. Environ. Manage.*, 2005, **75**, 275–282.

58 B. Aumont, S. Szopa and S. Madronich, Modelling the evolution of organic carbon during its gas-phase tropospheric oxidation: development of an explicit model based on a self generating approach, *Atmos. Chem. Phys.*, 2005, **5**, 2497–2517.

59 R. C. McVay, X. Zhang, B. Aumont, R. Valorso, M. Camredon, Y. S. La, P. O. Wennberg and J. H. Seinfeld, SOA formation from the photooxidation of α-pinene: systematic exploration of the simulation of chamber data, *Atmos. Chem. Phys.*, 2016, **16**, 2785–2802.